



# CHORUS

This is the accepted manuscript made available via CHORUS. The article has been published as:

## Diffusive transport through a model host-biofilm system

A. C. Aristotelous, I. Klapper, Y. Grabovsky, B. Pabst, B. Pitts, and P. S. Stewart

Phys. Rev. E **92**, 022703 — Published 10 August 2015

DOI: [10.1103/PhysRevE.92.022703](https://doi.org/10.1103/PhysRevE.92.022703)

# Diffusive Transport Through A Model Host-Biofilm System

A.C. Aristotelous,<sup>1</sup> I. Klapper,<sup>1,2,\*</sup> Y. Grabovsky,<sup>1</sup> B. Pabst,<sup>2</sup> B. Pitts,<sup>2</sup> and P.S. Stewart<sup>2</sup>

<sup>1</sup>*Department of Mathematics, Temple University*

<sup>2</sup>*Center for Biofilm Engineering, Montana State University*

**Abstract:** Free-living biofilms have been subject to considerable attention, and basic physical principles for them are generally accepted. Many host-biofilm systems, however, consist of heterogeneous mixtures of aggregates of microbes intermixed with host material and are much less studied. Here we analyze a key property, namely reactive depletion, in such systems and argue that two regimes are possible: (1) a homogenizable mixture of biofilm and host that in important ways acts effectively like a homogeneous macro-biofilm and (2) a distribution of separated microbiofilms within the host with independent local microenvironments.

**PACS numbers:** 87.18.Fx, 87.15.hj, 87.19.xb

## I. INTRODUCTION

Biofilms, collections of microorganisms living in self-secreted polymeric matrices, occur throughout natural and engineered systems and, wherever they occur, can significantly impact transport of many chemical quantities through reactive depletion or production mechanisms [1]. This influence is often the most important determining factor in how microbes interact with and affect their environment, and its consequences have been well documented under controlled, homogeneous conditions. A common consequence of transport in reactive-diffusive systems, central to biofilm function and ecology, is active layer formation [2]. As one example, though an especially important one, a thin, homogeneous layer of aerobic microbes (say 10-20  $\mu\text{m}$  thick) can rapidly deplete available oxygen, creating an anaerobic region, with resulting effects that can be profound in many instances [3, 4].

Formation of active layers is predicted in mathematical models as a consequence of interaction of diffusion and reaction [5]. For example, modeling biofilm as a layer  $z \in [0, H]$  with single substrate concentration  $C(z)$  satisfying

$$DC'' = r(C),$$

together with  $C(H) = C_0$ ,  $C'(0) = 0$ , see Figure 1, results in exponentially decaying substrate concentration for reasonable choices of reaction function  $r$  ( $D$  is a diffusion coefficient). That is, reaction depletes substrate within a layer near the exterior biofilm boundary  $z = H$ . Consequentially, the biofilm is divided into two environments, one with substrate available and one with substrate depleted, with a relatively sharp interface between them.

Reactive depletion and its effects have been extensively studied in *in vitro* lab settings. However, outside of the lab, microbial communities are generally uncontrolled and heterogeneous. This is particularly so for *in vivo* microbe-host interactions where biofilms often take the form of patchy aggregates, for example, in the mucus of the cystic fibrosis lung, on prosthetic joints, or in

chronic dermal wounds, and usually do not closely resemble *in vitro* biofilms [6, 7]. Generally, though, the dominant form of interaction between biofilm and host likely still involves diffusive transport, so active layer formation and its effects on that transport are as important in host-biofilm systems as elsewhere. Formation of anaerobic regions, for example, can have profound medical consequences for the host [8]. Complementarily, transport efficiencies can qualitatively affect microbial community function. Thus understanding the influence of local heterogeneity on large scale transport, although already of interest in pure biofilms, is particularly important in host-biofilm systems.

To address this issue, we hypothesize that aggregates of microbes distributed within a host could either effectively combine into a dense formation that acts like a homogeneous biofilm with similar reactive depletion properties, or else form a system of isolated aggregates with localized fluctuations (i.e., microenvironments) and altered impact on host-scale transport. We present empirical evidence for this and provide a theory to distinguish between effective host-microbe homogenization versus isolated within-host microbial colonies.

## II. METHODS

To approximate host-biofilm systems in a controlled setting, artificial host-biofilm mixes, called *gel-biofilms*, were formed by inoculating a green fluorescent protein expressing strain of *Staphylococcus aureus* (strain UAMS-1 containing plasmid pEM87 [9]) into liquid low melting temperature agarose and depositing small droplets on a glass-bottomed dish, see Figure 2(a)-(b). Oblate hemispheres were formed with a radius of approximately 680  $\mu\text{m}$ . 4 ml of 1/10-strength tryptic soy broth was added to the dish. The dish was placed in an environmental chamber on the stage of an inverted Leica TCS SP5 confocal scanning laser microscope and incubated at 37°C for 24 h. Specimens were stained with 40  $\mu\text{g}$  ml propidium iodide for 1 h then imaged on the confocal using standard FITC/TRITC fluorescence parameters and a 10x dry objective. Stacks of red and green fluorescent images were collected through the entire gel thickness, from

---

\* klapper@temple.edu

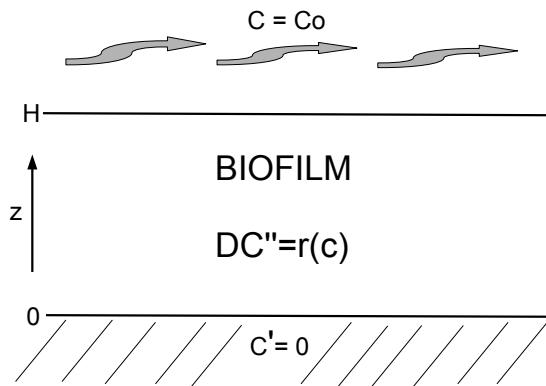


FIG. 1. One dimensional homogeneous biofilm model: substrate from an exterior region (where it is possibly replenished by a flow), diffuses and reacts in the biofilm region. Substrate concentration near  $z = 0$  may be small due to depletion via reaction in an active layer near  $z = H$ .

top to bottom and were analyzed using MetaMorph software (Molecular Devices). 22 images corresponding to the bottom 10% of the gel biofilm (adjacent to the glass attachment surface) were combined into a single projection. Average green (GFP, indicating anabolic activity) and red (propidium iodide, indicating cell mass independent of activity) intensities were computed in a series of concentric circles and normalized to area.

We introduce a mathematical model of diffusive transport and reaction in a host-biofilm system as follows. Substrate profile is determined by the reaction-diffusion equation

$$D\nabla^2 C = r(C)\chi(\mathbf{x}) \quad (1)$$

where  $C(\mathbf{x})$  is concentration of dissolved substrate and  $r$  is a reaction function [10]. Note the assumption of quasi-equilibrium – other than the diffusion-reaction equilibration time, the other time scale of principle interest, that of biological growth, is typically long in comparison. Also, we suppose that diffusivity  $D$  is independent of  $\mathbf{x}$ , reasonable for small molecules like oxygen. We do not expect qualitatively different results if  $D$  varies. The host domain is seeded randomly with circular microbial aggregates and the characteristic function  $\chi$  is defined to be 1 within aggregates and otherwise 0, i.e., reaction only occurs in aggregates. We employ a Monod form  $r(C) = \rho Y^{-1} \mu C / (K + C)$ .  $r$  has units of substrate concentration per time, and parameters in  $r$  are rate  $\mu$  ( $\text{time}^{-1}$ ), half-saturation  $K$  (substrate concentration), yield  $Y$  (cells per unit substrate), and  $\rho$  (cells concentration). Choices of parameter values, for both reaction function  $r$  and for aggregate distribution, have little effect on results except through key dimensional quantities described below. For generality we solve (1) in a rectangular host domain  $\Omega$ , defined by  $\mathbf{x} = (x, z) \in [0, L] \times [0, H]$ , with Dirichlet conditions  $C = C_0$  on the boundary  $z = H$  and no-flux conditions  $\nabla C \cdot \mathbf{n} = 0$  on the others (other

boundary conditions than no-flux do not have a significant effect on results).

To solve (1), a high-order discontinuous Galerkin (DG) finite-element (FE) numerical scheme with mesh refinement was employed. Since finite elements generate a variational formulation of (1), reactivity in the colony supported function  $\chi(\mathbf{x})$  can be efficiently captured using high-order numerical quadratures in conjunction with compatible meshes and isoparametric elements [11]. Curved microcolony boundaries were matched with elements that have curved boundaries (isoparametric elements) and adaptive mesh refinement. Mesh adaptivity was also employed to better resolve the effect of the aggregates on the oxygen profile [12]. A marking strategy [13–15] was used to drive the mesh adaptation. Adaptive mesh refinement is computationally challenging, so the DG method was used as it produces meshes with fewer degrees of freedom by allowing for hanging

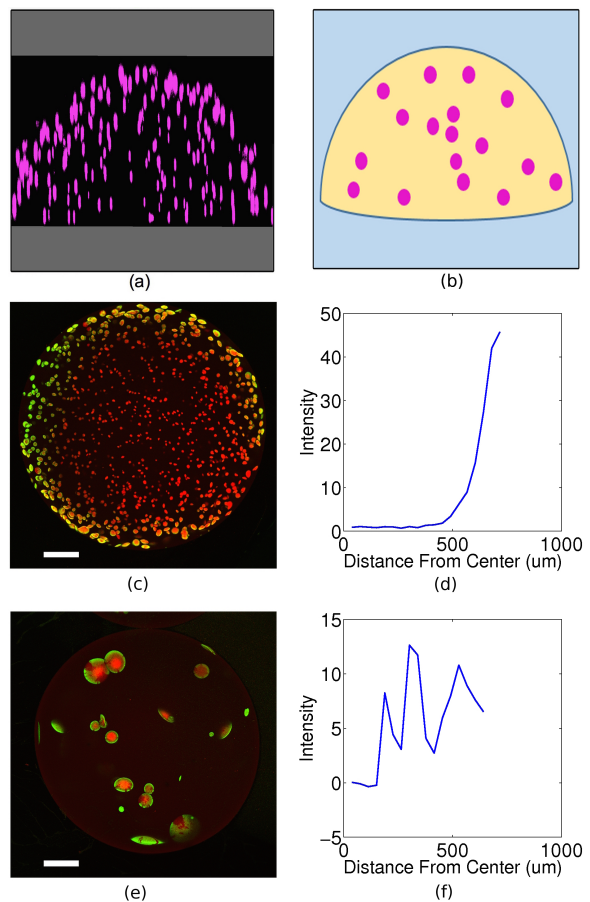


FIG. 2. (Color) (a) Sagittal confocal microscopy image of an example gel-biofilm (sideview), (b) diagram illustrating agarose gel (yellow) containing dispersed biofilm aggregates (magenta), grown for 24h, (c) bottom 10% of a densely colonized gel biofilm (topview), (d) its green fluorescence intensity, (e) bottom 10% of a sparsely colonized gel (topview), (f) its green fluorescence intensity. Scale bars are length  $200 \mu\text{m}$  in (c),(e).

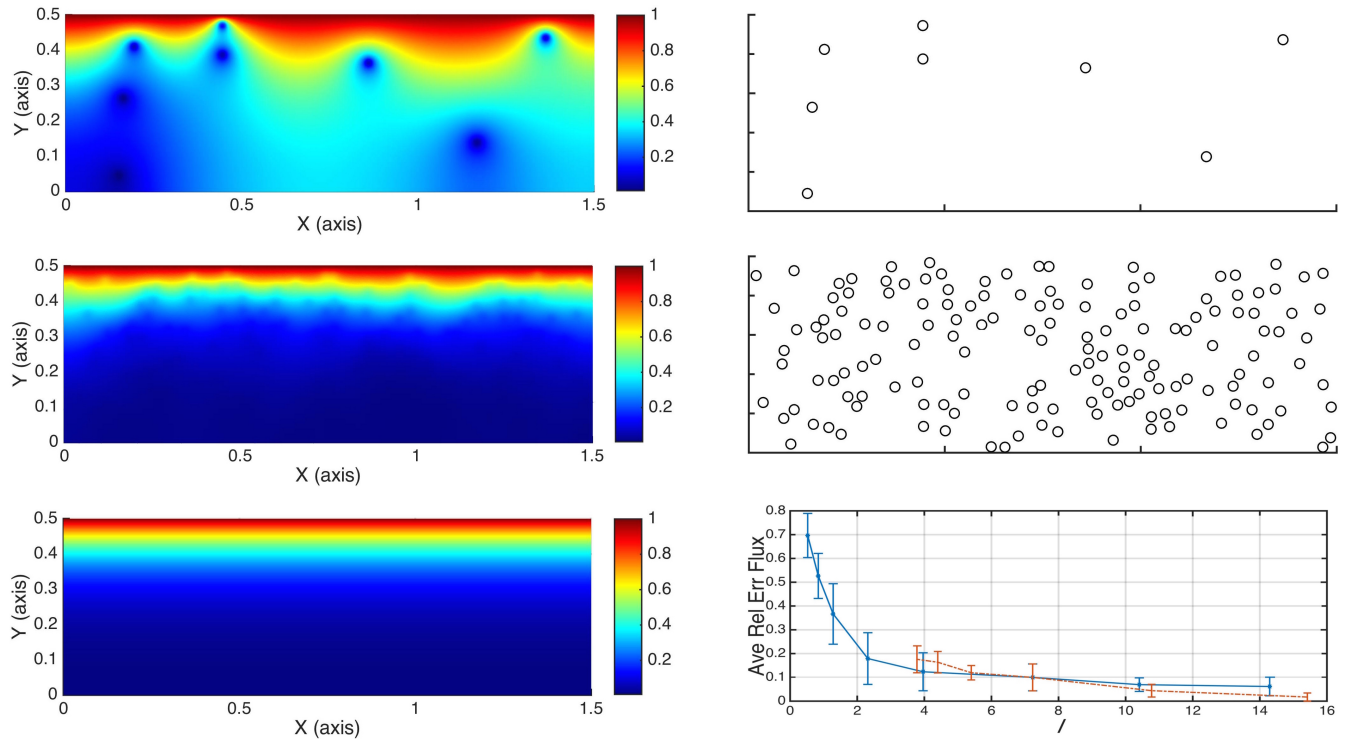


FIG. 3. (Color) Top row: a realization of a low volume fraction ( $\theta = 0.5\%$ ,  $I \approx 0.631$ ) substrate concentration profile (left) and micro-colony placement (right), with  $\ell = 0.198$ . Middle row: a realization of a high volume fraction ( $\theta = 10\%$ ,  $I \approx 6.62$ ) substrate concentration profile (left) and micro-colony placement (right), with  $\ell = 1.89 \times 10^{-2}$ . Bottom row: (left) substrate concentration for homogenized system, (right) averaged relative flux error  $(F_h - F)/F_h$  (over 20 realizations) versus  $I$ . (Blue)  $I$  varied by changing the number of micro-colonies with micro-colony reactivity fixed, (red)  $I$  varied by changing micro-colony reactivity with number of micro-colonies fixed. In all computations, colony diameter  $d = 0.025$  and effective active layer depth  $\lambda = 0.125$ .  $\lambda$ ,  $d$  and  $\ell$  are in units of domain height.

nodes, whereas continuous FE methods may require additional refinement or constraints in order to preserve mesh conformity. Specifically, due to its local nature, the DG-FE method allows quantities of interest to be expressed on single mesh elements without the requirement of additional globally prescribed conditions. An assortment of DG variants can be found in the literature [16].

The discrete DG approximation  $C_h \in V_h$  to the solution of (1) satisfies

$$\alpha_h(C_h, v_h) + (r(C_h)\chi(\mathbf{x}), v_h) = 0, \quad \forall v_h \in V_h \quad (2)$$

where  $v_h \in V^h$  is a DG basis function and  $V^h$  is the DG finite dimensional space consisting of piecewise polynomial elements [16]. Here the usual  $L^2$ -inner product is denoted by  $(\cdot, \cdot)$ , and  $\alpha_h(\cdot, \cdot)$  is the DG bilinear form corresponding to the Laplacian operator in variational form with prescribed BCs [17]. Third order DG basis polynomials provided  $O(h^4)$  accuracy in the  $L^2$ -norm of the spatial error at each time step, verified by Cauchy-convergence tests. Fixed-point inner iterations were used for the nonlinearities present in (2). Multilevel solvers tailored to the adaptive multilevel mesh were used to solve the linearized algebraic system arising from the numerical discretization. A conjugate gradient solver with

multigrid preconditioning (PCG) was employed [18–20]. Use of the symmetric interior penalty variant of DG-FE [16] resulted in symmetric positive-definite mass and stiffness matrices that have block structure benefiting the design of the iterative solver and preconditioner.

### III. RESULTS

Observations suggest a qualitative crossover, see Figure 2(c)-(f) for representative examples. As measured by microbial activity, a signature of oxygen penetration, densely placed microbial aggregates act as a homogeneously spread biofilm forming an active layer near the air-gel interface (Fig. 2(c)-(d)). However, when aggregates are sparsely distributed, isolated micro-biofilms show activity even far inside the gel, likely indicating deep penetration of oxygen (Fig. 2(e)-(f)).

To understand this behavior, we study model (1) of diffusive transport and reaction in a host-biofilm system. In agreement with measurements, the host-biofilm model also suggests qualitatively different behaviors, see Fig. 3: (A) the entire system acts effectively as a homogeneous biofilm or (B) individual microbiofilms function

effectively in isolation within the host. We explain using homogenization procedures, with the host-biofilm system being replaced by a homogeneous mixture [27]. Standard homogenization of (1) leads to equation

$$D \frac{d^2}{dz^2} C_h = r(C_h) \theta \quad (3)$$

for the homogenized concentration  $C_h$ , where  $\theta$  is the biofilm volume fraction (we suppose that  $\theta$  does not vary even on large scales, though this assumption can be relaxed). The host-biofilm system acts like a homogeneous biofilm at the macroscale if solutions of (3) are close to solutions of (1) in the sense that total substrate usage is similar. We use total substrate reaction rates  $\int_{\Omega} r(C) \chi d\mathbf{x}$  and  $\int_{\Omega} r(C_h) \theta d\mathbf{x}$  as a comparison statistic. Note that these rates reduce to fluxes into  $\Omega$  given, respectively, by  $F = D \int_{z=H} \partial C / \partial z dx$  and  $F_h = D \int_{z=H} dC_h / dz dx$ . Thus we compare the relative flux difference  $(F - F_h) / F_h$ .

The determining length here is  $\lambda = \sqrt{DC_0 / r(C_0) \theta}$ , roughly the depth to which substrate would penetrate before being reacted in a homogenized host-biofilm system, i.e., the effective active layer depth of the homogenized model (3). On the other hand, the local length scale is  $\ell$ , the heterogeneity scale, which we set to be a measure of the distance between microcolonies and is estimated by an average of all the the minimum distances between an individual aggregate and the rest. That is, for each of the  $m$  colonies,  $B_i$ ,  $i = 1, \dots, m$ , the minimum distance  $\ell_i$  between the boundaries  $\partial B_i$  and  $\partial B_j$  for  $j \neq i$  is calculated. Then,  $\ell$  is taken to be the average of  $\ell_i$ . For example, Figure 3, top and middle rows, correspond to  $\ell = 1.98 \times 10^{-1}$  and  $\ell = 1.89 \times 10^{-2}$ , respectively, in units of domain height.

We propose the nondimensional ratio  $I = \lambda / \ell$  as a homogenizability indicator. Large  $I$ , i.e., biofilm microcolonies close together relative to active layer depth, indicates that transport in the homogenized system is similar to that in the host-biofilm over large distances. Small  $I$ , i.e., biofilm microcolonies far apart relative to active layer depth, indicates that substrate fluctuations are significant, for example in the form of transport over large distances through the host-biofilm system. Large distance is quantified relative to the effective active layer depth.

Note that  $I$  might be considered to be a cousin to the commonly quoted Thiele modulus  $\Phi$ , a non-dimensional parameter that measures the ratio of a system (macro) length scale to the active layer depth  $\lambda$  [21, 22]. Typically,  $\Phi$  provides a measure of biofilm thickness in some general sense relative to a particular macroscale of interest [23–26].  $I$ , however, measures the ratio of  $\lambda$  to a system microscale  $\ell$  and so carries a different meaning, namely an indication of the importance of microscale heterogeneity on transport at larger scales. The domain defined Thiele modulus is pertinent here in one sense, though; we assume that the active layer depth  $\lambda$  is smaller than the domain depth  $H$ , i.e., that the Thiele modulus is greater

than 1. If not, diffusive transport is not significantly limited across the entire domain and the concept of an active layer is not applicable. For Thiele modulus less than 1, the appropriate indicator ratio would compare  $\ell$  with domain depth  $H$  rather than  $\lambda$ .

In Figure 3, we vary the volume fraction of the aggregates but also at the same time, importantly, their individual reactivity in such a way so as to keep the effective active layer depth constant at  $\lambda = 0.125$  in units of domain height (in particular,  $\mu$  is increased with decreasing volume fraction; similar results can be obtained varying other parameters). That is, though there are fewer aggregates in some simulations as compared to others, the total system reactive capacity is always the same, regardless. For each choice of volume fraction, 20 realizations are computed. In Figure 3 bottom right, average relative flux differences versus  $I$  is plotted. Observe that for low values of  $I$  the system is more heterogeneous and for high values of  $I$  the system is less heterogeneous. (The associated homogenized system for all computations in Fig. 3 has solution shown in the bottom left panel.) Thus the degree of heterogeneity can be effectively measured by  $I$ . Note consistency with empirically observed values in Table I. It is also illustrative to fix  $\ell$  and vary  $\lambda$ , see Figure 4 where the aggregate distribution is unchanged from computation to computation but instead aggregate reactivity varies. Fig. 4 demonstrates that the “eye test” (effectively, comparison of heterogeneity scale  $\ell$  to system scale  $L$ ) fails – knowing only the aggregate density and placement is not sufficient to predict homogenizability. Rather, heterogeneity scale  $\ell$  must be considered in comparison to the effective active layer length  $\lambda$ , which is not possible by eye.

Note that, in Fig. 3 bottom right, error bars for the blue curve ( $I$  varied by changing number of microcolonies, with micro-colony reactivity fixed) and for the red curve ( $I$  varied by changing micro-colony reactivity, with micro-colony number fixed) overlap, supporting the claim that the non-dimensional ratio  $I$  is the determining quantity. Also note two computational limitations: (1) it is difficult to extend the red curve to  $I \lesssim 4$  because of the large reactivities that would be required, and (2) large  $I$  values on the blue curve are somewhat suspect due to the requirement for large numbers of micro-colonies. In this second instance, the fixed micro-colony radius causes excluded volume effects that likely lead to under-population of biofilm material near the top,  $z = H$  boundary, thus artificially increasing diffusive transport resistance and so reducing flux.

Values of  $I$  for the experiments shown in Fig. 2 can be estimated [28], see Table I. Classical chemical engineering theory predicts the flux of a reactant into catalytic aggregates in terms of the effectiveness factor ( $\eta$ ) and Thiele modulus (here taken as  $\Phi = \text{droplet radius} / \text{active layer depth}$ ) [22]. Useful bounds on the behavior of Monod kinetics, assumed in this work, are provided by zero order ( $\eta_0 = 1 - (1 - 1/\Phi)^3$  for  $\Phi > 1$ ) and first order ( $\eta_1 = (3/\Phi^2)(\Phi \coth \Phi - 1)$ ) kinetic results. Values for

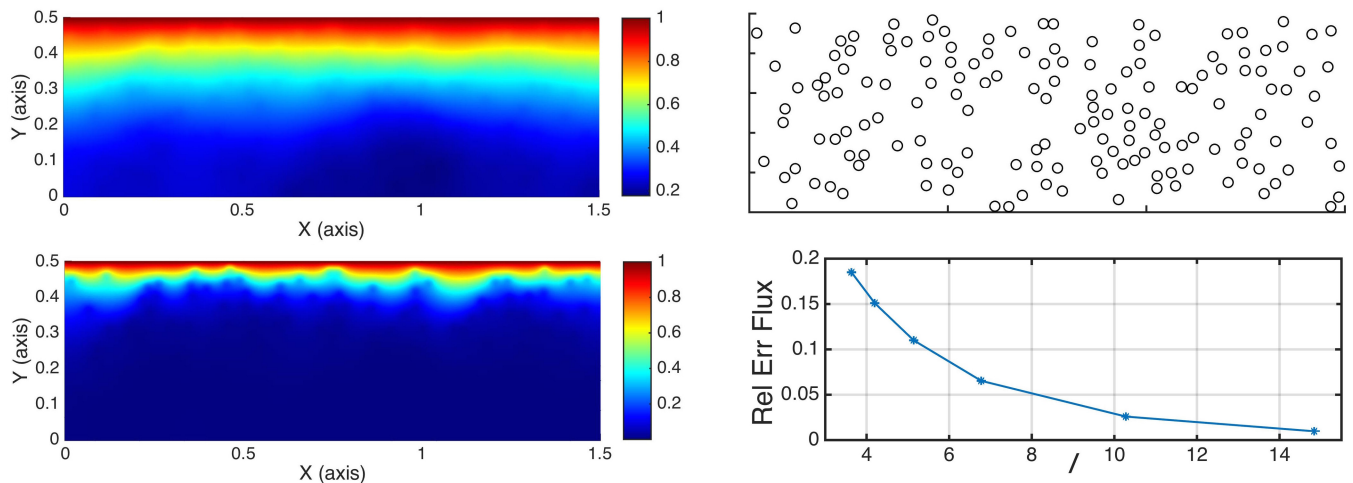


FIG. 4. (Color) As in Fig. 3 except varying  $\lambda$  instead of  $\ell$ . Top right: aggregate placement used for all computations, same as shown in Fig. 3, middle row. Bottom right: resulting relative flux error as a function of  $I$ . Left column: two solutions, with  $\lambda = 0.274$ ,  $I = 14.8$  (top) and  $\lambda = 0.0670$ ,  $I = 3.6$  (bottom),  $\lambda$  given in units of domain height. Note that bottom left shows flux error for a single micro-colony realization (that shown in top right). Average flux error of an ensemble of realizations is shown in Figure 3, bottom right, red curve.

Exp.	Image	$\ell$ ( $\mu\text{m}$ )	$\theta$	$\lambda$ ( $\mu\text{m}$ )	R ( $\mu\text{m}$ )	$I$	$\eta_0$	$\eta_1$	$\eta_{\text{exp}}$	err
1 (denser)	Fig. 2(a)	5.3	0.198	71	706	13	0.385	0.385	0.375	0.025
2 (sparser)	Fig. 2(c)	72	0.071	118	654	1.6	0.449	0.443	0.407	0.09

TABLE I.  $\ell$ ,  $\theta$ ,  $\lambda$ , and resulting  $I$ , as well as efficiencies and errors, for gel biofilms shown in Fig. 2.

these predictions, which correspond to the homogenized flux in dimensionless form, are given in Table I along with an experimental estimate of the actual effectiveness factor calculated from the images in Fig. 2 by integrating the green intensity over the hemisphere and dividing by the product of maximum green intensity and volume fraction. The values of  $\eta_0$  and  $\eta_1$  for the denser gel biofilm (Fig. 2(c)) were corrected by multiplying by  $\sqrt{2}$  to account for the non-uniform distribution of biomass which was approximately twice as dense in the active region of the gel biofilm compared to the average density. Consistent with the theory developed here, the error incurred by homogenization was larger for the sparser aggregate, which had a smaller value of  $I$ .

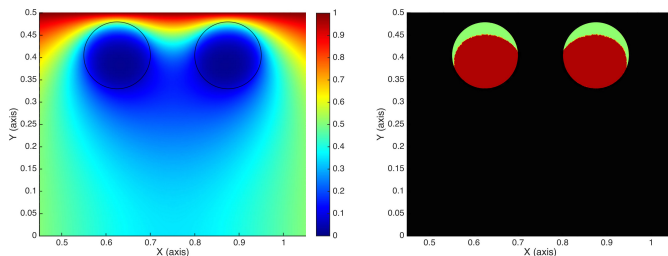


FIG. 5. (Color) Left: realization with two colonies,  $I = 1.25$ . Right: same computation except colored as in Fig. 2 with active (green) and inactive (red) biomaterial.

#### IV. DISCUSSION

Host-biofilm systems, and even biofilms themselves, are heterogeneous materials. For large scale physical phenomena, effective averaging of heterogeneity is appropriate when small scale variation does not play an important, direct role at the macroscale, at least for questions of transport. It is argued here that such is the case when the heterogeneity scale is small compared to the active layer depth, in which case the system acts, at least for purposes of transport, like a “classical” biofilm. When homogenization is not appropriate, however, i.e., when the heterogeneity scale is significant, then fluctuations cannot be neglected. Such fluctuations can lead to microenvironment formation even within individual aggregate, e.g. compare Fig. 2 and Fig. 5, which can lead to phenomena not seen in homogenized systems. (Relatedly, interactions between leucocytes and microcolonies can result in local active layers with inner depleted oxygen zones with significant consequences [29].) Local variation occurs at a third length scale, the local active layer depth  $\lambda_L = \sqrt{DC_0/r(C_0)}$ , and can become important when  $\lambda_L/\lambda = \sqrt{\theta}$  is small. However,  $\sqrt{\theta} \sim \ell^{-d/2}$ , so that small  $\lambda_L/\lambda$  requires small  $I$  and thus significant fluctuations are not expected to occur in the homogenizable regime. Note, localized active layers and depletion zones are seen in non-homogenizable systems, see Fig. 2 and Fig. 5.

Biofilm function, and that of naturally occurring mi-

icrobial communities generally, is closely coupled to environment. When that environment is a host system, it is important to understand how transport in and out of the community is affected. Indeed, this can be the most important physical characteristic in the context of overall system function and hence characterization of homogenizability is a necessary starting point for understanding form and function of biofilms in host systems. The difference between homogenizability versus non-homogenizability has important consequences; reductions and alterations in transport in a biofilm dominated system may significantly degrade host function, including ability of the host to defend against biofilm infection [30]. Further, beyond statics, there are also implications for dynamical properties: while biofilms are

generally considered as chronic, the fact that they are actively growing (or possibly, in the presence of host response, decaying) systems also presents the possibility of transitions and bistability [31] between transport active and reactive depleted dynamics resulting in acute presentations.

## ACKNOWLEDGMENTS

The authors wish to acknowledge support from NIH award R01GM109452. Microscopy was made possible by equipment funded by the M. J. Murdock Charitable Trust and NSF award 1039785.

- 
- [1] W.G. Characklis, Fouling biofilm development: A process analysis, *Biotech. Bioeng.* **23**, 1923-1960 (1981).
- [2] P.S. Stewart, M.J. Franklin, Physiological heterogeneity in biofilms, *Nature Reviews Microbiology* **6**, 199-210 (2008).
- [3] P.S. Stewart, Diffusion in biofilms, *Journal of Bacteriology* **185**, 1485-1491 (2003).
- [4] M. Staal et al., Ultrabright planar optodes for luminescence life-time based microscopic imaging of O<sub>2</sub> dynamics in biofilms, *Microb. Methods* **85**, 67-74 (2011).
- [5] I. Klapper, Productivity and equilibrium in simple biofilm models, *Bull. Math. Biol.* **74**, 2917-2934 (2013).
- [6] T. Bjarnsholt, Maria Alhede, Morton Alhede, S.R. Eickhardt-Sørensen, C. Moser, M. Kühl, Ø.P. Jensen, and N. Høiby, The *in vivo* biofilm. *Trends in Microbiology* **21**, 466-474 (2013).
- [7] P.S. Stewart, Biophysics of biofilm infection, *Pathogens and Disease* **70**:212-218 (2014).
- [8] D. Worlitzsch et al., Effects of reduced mucus oxygen concentration in airway *Pseudomonas* infections of cystic fibrosis patients, *J. Clin. Invest.* **109**, 317-325 (2002).
- [9] D.E. Moormeier, J.L. Endres, E.E. Mann, M.R. Sadykov, A.R. Horswill, K.C. Rice, P.D. Fey, and K.W. Bayles, Use of microfluidic technology to analyze gene expression during *Staphylococcus aureus* biofilm formation reveals distinct physiological niches. *Appl. Environ. Microbiol.* **79**, 3413-3424 (2013).
- [10] I. Klapper, J. Dockery, Mathematical description of microbial biofilms, *SIAM Rev.* **52**, 221-265 (2010).
- [11] D.A. Di Pietro, A. Ern. *Mathematical Aspects of Discontinuous Galerkin Methods*. Springer, Berlin (2012).
- [12] A.C. Aristotelous, M.A. Haider. Use of Hybrid Discrete Cellular Models for Identification of Macroscopic Nutrient Loss in Reaction-Diffusion Models of Tissues. *Int. J. Numer. Meth. Biomed. Engng.*, **30**(8), 767-780 (2014).
- [13] J.L. Bona, V.A. Dougalis, O.A. Karakashian, W.R. McKinney. Fully discrete methods with grid refinement for the generalized Korteweg-de Vries equation. *Proc. of the workshop on viscous and numerical approximations of shock waves, NCSU*, 117-124 (1990).
- [14] J.L. Bona, V.A. Dougalis, O.A. Karakashian, W.R. McKinney. Conservative high order schemes for the Generalized Korteweg-de Vries equation. *Philos. Trans. Royal Soc. London, Ser.*, **351**, 107-164 (1995).
- [15] A.C. Aristotelous, O.A. Karakashian, S.M. Wise. Adaptive, Second-Order in Time, Primitive-Variable Discontinuous Galerkin Schemes for a Cahn-Hilliard Equation with a Mass Source. *IMA J. Numer. Anal.* **10.1093/imanum/dru035** (2014).
- [16] D.N. Arnold, F. Brezzi, B. Cockburn, L. D. Marini. Unified analysis of discontinuous Galerkin methods for elliptic problems. *SIAM J. Numer. Anal.*, **39**, 1749-1779 (2002).
- [17] B. Rivière. *Discontinuous Galerkin Methods for Solving Elliptic and Parabolic Equations*. SIAM, Philadelphia (2008).
- [18] A.C. Aristotelous, O.A. Karakashian, S.M. Wise. A Mixed Discontinuous Galerkin, Convex Splitting Scheme for a Modified Cahn-Hilliard Equation and an Efficient Nonlinear Multigrid Solver. *DCDS-B*, **18**(9), 2211-2238 (2013).
- [19] J.H. Bramble. *Multigrid Methods*. Research Notes in Mathematics Series. Chapman and Hall/CRC, London (1993).
- [20] S.C. Brenner, L.Y. Sung. Multigrid algorithms for  $c^0$  interior penalty methods. *SIAM J. Numer. Anal.*, **44**, 199-223 (2006).
- [21] E. Thiele. Relation between catalytic activity and size of particle. *Ind Eng Chem* **31**, 9169-920 (1939).
- [22] R.B. Bird, W.E. Stewart, E.N. Lightfoot. *Transport Phenomena*. John Wiley & Sons, New York, NY (2002).
- [23] P.S. Stewart, Theoretical aspects of antibiotic diffusion into microbial biofilms, *Antimicrob. Agents* **40**, 2517-2522 (1996).
- [24] C. Picioreanu, M.C.M. van Loosdrecht, J.J. Heijnen. Effect of diffusive and convective substrate transport on biofilm structure formation: a two-dimensional modeling study. *Biotech. Bioeng.* **69**, 504-515 (2000).
- [25] J. Dockery, I. Klapper, Finger formation in biofilm layers, *SIAM J. Appl. Math.* **62**, 853-869 (2002).
- [26] C. D. Nadell, K. R. Foster, J. B. Xavier. Emergence of spatial structure in cell groups and the evolution of cooperation. *PLoS Comput Biol* **6**, e1000716 (2010).
- [27] G. Papanicolau, A. Bensoussan, J.-L. Lions. *Asymptotic Analysis for Periodic Structures*, Elsevier (1978).
- [28] Analysis was performed on images to extract estimates of

- average cluster nearest neighbor distance ( $\ell$ ) and volume fraction occupied by clusters ( $\theta$ ). To estimate  $\lambda$ , previously published estimates of active layer depth in a colony biofilm of *S. aureus* ( $\theta = 1$ ,  $\lambda \approx 31.5\mu\text{m}$ ) were used, see Rani, S. A., Pitts, B., Beyenal, H., Veluchamy, R. A., Lewandowski, Z., Davison, W. M., Buckingham-Meyer, K., and P. S. Stewart. Spatial patterns of DNA replication, protein synthesis, and oxygen concentration within bacterial biofilms reveal diverse physiological states. *J. Bacteriol.* **189**, 4223-4233 (2007).
- [29] M. Kolpen et al., Polymorphonuclear leucocytes consume oxygen in sputum from chronic *Pseudomonas aeruginosa* pneumonia in cystic fibrosis, *Thorax* **65**, 57-62 (2010).
- [30] H.W. Hopf, Hunt TK, West JM, Blomquist P, Goodson WH 3rd, Jensen JA, Jonsson K, Paty PB, Rabkin JM, Upton RA, von Smitten K, Whitney JD. Wound tissue oxygen tension predicts the risk of wound infection in surgical patients. *Arch. Surg.* **132**, 997-1004 (1997); M. Schobert, P. Tielen, Contribution of oxygen-limiting conditions to persistent infection of *Pseudomonas aeruginosa*. *Future Microbiol.* **5**, 603-621 (2010).
- [31] T. Bjarnsholt, P.Ø. Jensen, M.J. Fiandaca, J. Pedersen, C.R. Hansen, C.B. Andersen, T. Pressler, M. Givskov, N. Høiby, *Pseudomonas aeruginosa* biofilms in the respiratory tract of cystic fibrosis patients, *Pediatr Pulmonol* **44**, 547-558 (2009).